buildings

MDPI

Article

Experimental Investigation and Design of Novel Hollow Flange Beams under Bending

Jingya Xue [1], Shiliang Ma [2], Xiaomiao Chen [1,*], Qing Wu [1], Yifan Wang [1], Yunqing Wang [3], Muhammad Akbar [4] and Ning Yang [5]

[1] School of Civil Engineering and Architecture, Jiangsu University of Science and Technology, Zhenjiang 212100, China
[2] Zhenjiang University Park Headquarters, Zhenjiang 212100, China
[3] Plais Precision Technology (Shenzhen) Co., Ltd., Shenzhen 518110, China
[4] Institute of Mountain Hazards and Environment, Chinese Academy of Sciences, Chengdu 610041, China
[5] China Coal Technology Engineering Group, Coal Industry Planning Institute, Beijing 100120, China
* Correspondence: cxm2020@just.edu.cn

Abstract: In this paper, a new type of assembling rivet-fastened rectangular hollow flange beams (ARHFBs) is proposed. The cross-section of the ARHFB consists of two U-shaped and C-shaped components connected by self-locking rivets to form two rectangular hollow flanges. To study the performance and strength of the ARHFB as a flexural member, eight four-point bending tests and more than 40 simulation studies were carried out. The details, results, and comparison of the four-point bending tests, especially the characteristics of the test bench and the lateral support, are presented in this paper. ARHFB sections with varied rivet spacing, web depth, and flange width were experimentally studied. Additionally, a parametric study of ARHFB was conducted using finite element models verified by test results. The influence of span on the loading capacity of ARHFB was discussed. ARHFB can be used in large-span buildings. A more economical ARHFB component selection method was given. The depth of the flange, the strength of the web, and the thickness of the web are important parameters of ARHFB. The loading capacity obtained from the test was compared with the predicted values of the design formulas in the American Iron and Steel Institute (AISI) and the Chinese design standard for cold-rolled steel (GB50018). The calculation and verification of ARHFB flange buckling and lateral torsional buckling were also considered. It is recommended that GB50018 be used to predict the flexural capacity of ARHFBs.

Keywords: cold-formed steel; experimental investigation; hollow flange beam; rivet-fastened

check for updates

Citation: Xue, J.; Ma, S.; Chen, X.; Wu, Q.; Wang, Y.; Wang, Y.; Akbar, M.; Yang, N. Experimental Investigation and Design of Novel Hollow Flange Beams under Bending. *Buildings* **2024**, *14*, 1413. https://doi.org/10.3390/buildings14051413

Academic Editor: Humberto Varum

Received: 9 April 2024
Revised: 25 April 2024
Accepted: 8 May 2024
Published: 14 May 2024

1. Introduction

As a widely used construction material, steel has many advantages such as high strength, light weight and good mechanical properties, and the steel structure also has good seismic performance [1,2]. Cold-formed thin-walled steel structures have the above advantages of steel, a higher strength-to-weight ratio and easier processing and installation methods than traditional steel structures. In steel structures, the I-section is a well-known type of section with high stiffness in the plane of applied loads. However, this type of section has low lateral and torsional stiffness and is susceptible to overall instability, thus reducing the flexural capacity of the I-beam. That is to say, the strength of the steel is not fully utilized. In light of this, in the 1980s, cold-formed thin-walled triangular hollow flange beams (HFB) with closed triangular flanges were proposed by Palemer Tube Milles, Australia [3]. Using hollow flanges instead of conventional plates overcame the problem of weak torsional stiffness of the traditional I-section, resulting in a significant improvement in the overall stability of the beam. At this point, local buckling becomes a major factor in the instability of hollow flange beams due to their relatively frangible webs. Therefore, this paper proposes a beam section form with a hollow flange using rivets assembled (ARHFB)

to utilize and extend light steel construction and hollow flange section advantages. This cross-sectional form of beams allows for the selection of flanges and webs with different strengths according to the requirements, thus substantially increasing the utilization of steel. The torsional stiffness of the cross-section is further increased, and the possible local buckling of the web is reduced. Additionally, with the use of self-locking rivets for the connection between cold-formed thin-walled steel components, the advantages of easy processing and installation of light steel structures are maintained. The cross-sectional properties of assembling rivet-fastened rectangular hollow flange beams (ARHFBs) and the applicability of existing specifications to ARHFBs need to be further studied.

Lightweight steel has been used as the load-bearing skeleton of buildings since the 1950s [4]. Cold-formed thin-walled steel profiles are the main material for making lightweight steel structures and are produced in two ways: hot-rolled and cold-rolled. Various cross-sections formed by processing include C-shaped, U-shaped, L-shaped, etc. The tensile strength of such cold-formed steel sections is improved compared to ordinary steel components. According to He et al. [5], under the same cross-sectional area, the radius of gyration of cold-formed steel increases by more than 50%, and the moment of inertia also increases by 50–180%. This has led to extensive research on the application of cold-formed steel, and steel beams with hollow flanges were subsequently proposed. Dempsey et al. [6] investigated the elastic buckling deformation of hollow flange beams (HFBs) by finite element analysis. A design method for HFBs was proposed based on the specification AS/NZS 4600. Hassanein MF et al. studied the shear behavior of I-shaped steel beams with rectangular hollow steel channels on both the top and bottom flanges. The results of the study showed that the predictions for rectangular hollow flange beams in Eurocode EC3 were conservative, and, as a result, the design equations in EC3 were modified [7]. To observe the behavior and strength of a uniaxially symmetric LiteSteel beam (LSB) as a flexural member, Anapayan et al. [8] conducted more than 50 transverse buckling tests. The study pointed out that the LSB undergoes transverse torsional buckling along with transverse deflection, torsion, and web twist. The test results were compared with the design code in AS/NZS 4600, and a moment discount factor was proposed to modify the existing formula. Hassaneind [9] carried out a parametric analysis on the shear performance of biaxially symmetric rectangular hollow tubular flange plate girders (HTFPGs), then compared the effect of important parameters such as flange width-to-depth ratio and web aspect ratio for the Eurocode standard EN 1993-1-5 [10]. The relative relationship between the actual flange yield strength and the considered original value ($f_{yf}/355$) was shown by finite element analysis to be an important factor affecting the shear strength of the beams, leading to an improvement of the traditional formulae in the code. The flexural capacity of the hollow tubular flange plate girders (HTFPGs) was compared with that of the traditional I-beam IPG. The results showed that HTFPG possesses a higher critical moment. This has led to a significant increase in research on hollow flange girders [11]. In order to better predict the flexural performance of beams with hollow flanges and to find design equations that can accurately estimate the bending capacity of the beams, Hassaneind et al. [12] studied the design codes of the American Institute of Steel Construction (AISC) and found that the assumptions made in the AISC for the bending moment gradient were conservative. Therefore, extensive finite element analyses were carried out to determine more reliable values of moment gradients, from which the design equations in AISC were modified. To better predict the flexural performance of beams with hollow flanges using the American Institute of Steel Construction (AISC), Mohebkhah et al. compared the FEA results of lateral torsional buckling capacity of triangular hollow flange I-beams with the prediction results of AISC, and it was pointed out that the moment gradient factor and the moment load carrying capacity prediction curves for the material given in AISC are conservative. Therefore, a new design equation for the material moment gradient factor is given to modify the AISC prediction results [13]. In addition, in the steel structure construction industry, various members need to be assembled into a whole by welding, bolting, riveting, etc., and therefore, much research has been conducted on

built-up sections. Gregory Kenneth Peters [14] experimentally investigated the moment carrying capacity of a built-up closed section consisting of a C-shaped section collocated with a U-shaped section. Abbasi M [15] analyzed the stability of cold-formed built-up sections using the composite strip method by incorporating the stiffnesses associated with the connected units into the overall stiffness matrix of the built-up section. This provides a method for calculating the load-carrying capacity of combined steel members. However, the existing design formulas often fail to predict the load-carrying capacity of combined cold-formed steel members with intermittent connections, as the intermittently connected assemblies are not accounted for in the steel design codes.

In this study, a new cross-section form with closed rectangular hollow flanges composed of C-shaped and U-shaped steel components connected by self-piercing rivets (ARHFB) is proposed to avoid web distortion and to improve steel utilization, as shown in Figure 1. Specimen connection using ST3 × 5 self-locking rivets was used in order to understand the strength of the connection point of the selected 1.5 mm thick Q235 galvanized for the Taguchi test; the results show that the tensile strength of the connection point is 3.8 KN. This cross-section form allows for the selection of flanges and webs of different sizes, thicknesses, and yield strengths according to the project requirements. It allows for assembling on the construction site due to the convenient installation method of lock riveted connections. This paper conducted experimental studies investigating the flexural performance of assembling rivet-fastened hollow flange beams (ARHFBs). An effective finite element model has been developed based on tests at quarter loading points. A built-up section of flanges and webs with different strengths has been analyzed using finite element analysis. The relationship between rivet spacing and the resulting decay in capacity was also discussed. Important parameters affecting the loading capacity of the ARHFBs were identified based on the tests and finite element analysis. In order to find a more suitable design code for predicting the loading capacity of the ARHFBs, this paper predicts the bending performance of ARHFBs using the design equations given in the Chinese design standard for cold rolled steel sections (GB50018) [16] and American Iron and Steel Institute (AISI) [17]. In addition, corresponding recommendations are made.

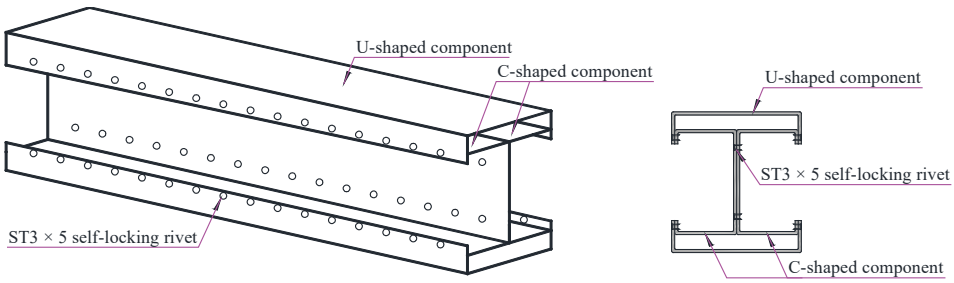

Figure 1. Construction of the specimen and section form.

2. Experimental Investigation

2.1. Test Specimen

The newly assembled hollow flange beam (ARHFB) proposed in this study comprises two U-shaped components and two C-shaped components. Self-locking rivets first connect the two C-shaped components, and then the U-shaped components are connected with C-shaped components to form a hollow flange beam with a closed section. An experimental study was carried out by applying the load at a quarter of the loading point to investigate the flexural behavior of a new type of assembling rivet-fastened hollow flange beam (ARHFB). A four-point bending test was selected to study the bending behavior of the pure bending section of the beam. Specifically, a total of eight four-point bending tests were carried out. When ARHFB is in a pure bending state, the bearing capacity and failure mode will be affected by many parameters, including flange depth ($d_{f0} - d_{f1}$), flange width (b_f), flange thickness (t_f), web depth (d_w), and web thickness (t_w) marked in Figure 2. Eight ARHFB specimens with different sizes are designed, as shown in Table 1. Table 1

lists the sample labels, the actual dimensions of the measured ARHFB parameters, and the nominal cross-sectional dimensions. Self-locking rivets are used for connection. Self-locking rivets have three kinds of connection spacing: 100 mm, 150 mm, and 200 mm. Among them, the ARHFBs connected by different rivet spacing have different numbers of rivets: 100 mm rivet spacing (96), 150 mm rivet spacing (66), and 200 mm rivet spacing (48). In these details, the length of the cold-formed thin-walled steel beam (L) and the size of the self-locking rivet (ST5.3 × 5.5) remain unchanged. The net distance (L_{span}) of the specimen length is designed as the distance between the left and right support points, which is 1500 mm. All the components that make up the ARHFBs, including U-shaped and C-shaped steel members, were made of Q235-grade steel.

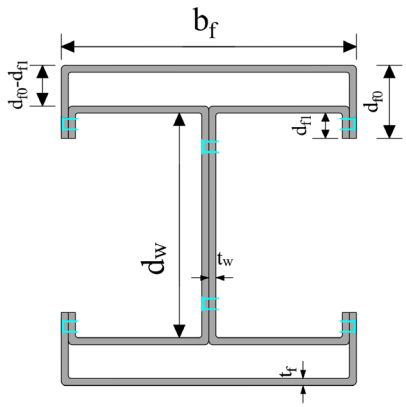

Figure 2. Cross-sectional notations for assembled rectangular hollow flange beams (ARHFBs).

Table 1. Measured dimensions of rivet-fastened assembled rectangular hollow flange beams (ARHFBs).

No.	Rivet Spacing (mm)	ARHFB Sections $d_w \times b_f \times d_{f0} - d_{f1} \times t_f \times t_w$ (mm)	L (mm)	L_{span} (mm)	d_w (mm)	Top b_f (mm)	Bottom b_f (mm)	Top $d_{f0} - d_{f1}$ (mm)	Bottom $d_{f0} - d_{f1}$ (mm)
1	100	140 × 150 × 30 × 1.5 × 1.5	1700	1500	140.36	151.26	150.93	30.28	30.48
2		140 × 170 × 30 × 1.5 × 1.5	1700	1500	139.16	170.31	170.69	30.40	30.37
3		140 × 170 × 30 × 2 × 2	1700	1500	141.28	170.62	170.08	30.42	30.18
4		140 × 170 × 40 × 1.5 × 1.5	1700	1500	140.54	169.59	170..67	40.31	39.96
5		170 × 170 × 30 × 1.5 × 1.5	1700	1500	170.32	170.48	170.22	30.54	30.51
6		170 × 170 × 30 × 1.5 × 2	1700	1500	170.08	170.83	169.93	29.72	30.37
7	150	140 × 150 × 30 × 1.5 × 1.5	1700	1500	140.13	150.37	150.31	30.78	30.06
8	200	140 × 150 × 30 × 1.5 × 1.5	1700	1500	139.47	149.83	150.16	29.96	30.54

In order to study the influence of rivet spacing on the bearing capacity of ARHFBs, a comparative test was carried out on the specimen 140 × 150 × 30 × 1.5 × 1.5 with 100 mm rivet spacing and 150 mm and 200 mm rivet spacing. In addition, the specimen 140 × 150 × 30 × 1.5 × 1.5 was compared with the specimen 140 × 170 × 30 × 1.5 × 1.5 to study the influence of flange width. The specimen of 140 × 170 × 30 × 1.5 × 1.5 was used as the comparison group, compared with the specimen of 140 × 170 × 30 × 2 × 2 and the specimen of 170 × 170 × 30 × 2 × 1.5 to study the effect of flange and web thickness on the bending behavior under pure bending. Then, compared with the specimens 140 × 170 × 40 × 1.5 × 1.5 and 170 × 170 × 30 ×1.5 × 1.5 to study the influence of flange and web depth.

2.2. Measurement of Initial Imperfection

Before the test, the initial defects of each component in the sample were measured to determine the error caused by the processing technology. This will affect the overall stability of the assembled hollow flange beam (ARHFB). Studying the overall buckling of purely curved sections of beams is important. Therefore, to obtain more accurate initial

defects of each component in the beam, the surface of each component is divided into 100 mm × 100 mm grids. According to the four vertices of the square grid, 15–17 measuring points are marked on each surface of the sample. During the measurement, a straight line is formed at both ends of the component fixed with a G-type clamp. The distance between the points on both sides of the corresponding position of the component is measured by the vernier caliper, and the average value of each measuring point is recorded as the initial geometric defect of the corresponding position of the component. Each component is measured twice and averaged. Table 1 lists the initial geometric imperfections at different positions of all specimens. According to the measurement results, the width of the flange varies from 149.83 to 170.83, the depth varies from 49.61 to 60.47, and the thickness varies from 1.26 to 2.11. The width of the web varies from 74.86 to 75.21, the depth varies from 139.16 to 170.32, and the thickness varies from 1.52 to 1.99.

2.3. Materials Properties and Geometric Calculation of Cross-Sections

Tensile specimens were prepared from U-shaped and C-shaped cold-formed thin-walled steel members, respectively. According to the 'Metallic Materials-Tensile Test Part 1: Test Methods at Room Temperature' (GB/T228.1-2010) [18], a standard tensile specimen was designed, as shown in Figure 3. Eight plate specimens (Figure 4) were taken from the plate parallel to the rolling direction for the tensile test. Among them, two kinds of C-shaped and U-shaped cold-formed thin-walled steel plates with thicknesses of 1.5 mm and 2 mm were taken. The tensile test was carried out using a 100 KN microcomputer-controlled tensile testing machine (Figure 5). The 100 KN microcomputer-controlled tensile testing machine adopts displacement-controlled loading. When the steel yield limit is not reached, the loading speed is 0.1 mm/min. After reaching the yield strength of the stress–strain curve, the loading speed is 0.5 mm/min. In the tensile test, the two ends of the tensile specimen are first fixed on the fixture of the microcomputer-controlled tensile testing machine, and an electronic extensometer is installed on the sample to obtain the deformation elongation of the tensile specimen, as shown in Figure 6. The tensile test results of different thicknesses of the two components are averaged and shown in Table 2. The stress–strain curve of the steel is shown in Figure 6.

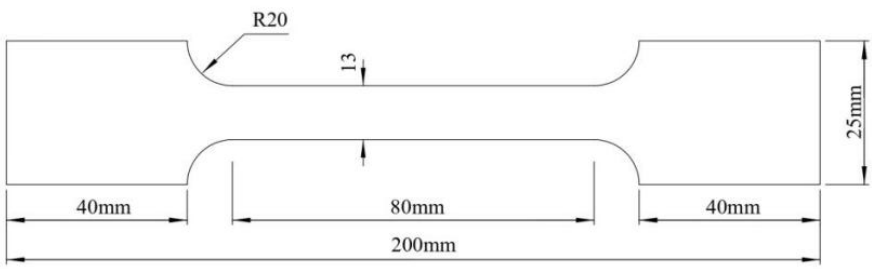

Figure 3. Details of the tensile coupon.

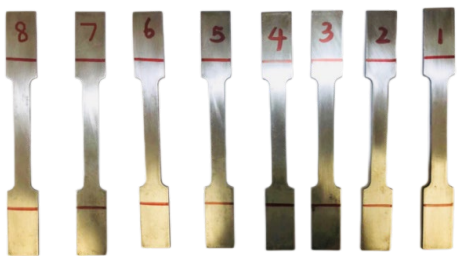

Figure 4. Tensile coupons before testing.

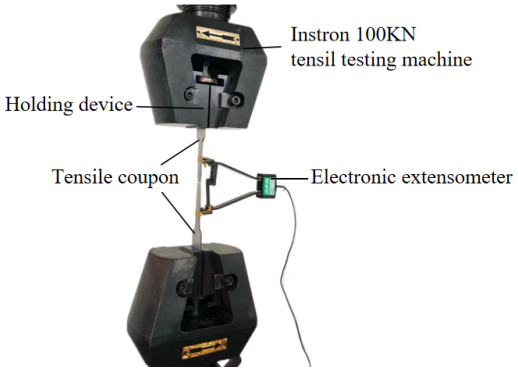

Figure 5. Tensile coupon test setup.

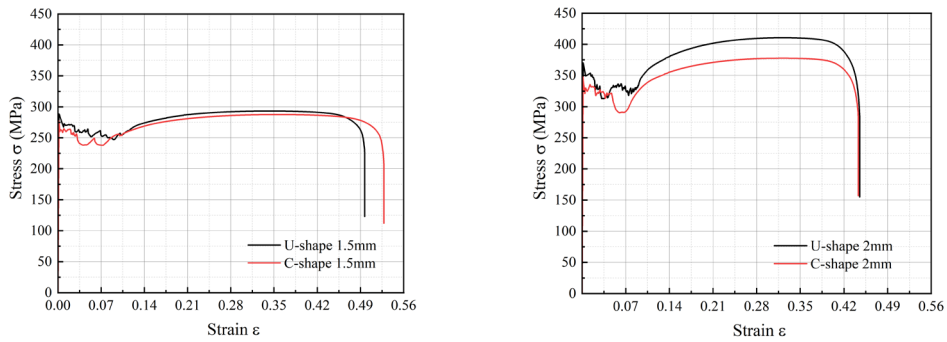

(**a**) 1.5 mm thick steel plate (**b**) 2 mm thick steel plate

Figure 6. Typical stress–strain for two thicknesses.

Table 2. Key average material properties for Q235 steel from tensile coupon tests.

Component Type	Steel Thickness	E	f_y	f_u	ε_y	ε_{sh}	ε_u	ε_f	f_u/f_y
	mm	N/mm^2	N/mm^2	N/mm^2	%	%	%	%	-
U-shape	1.5	215,753	288.48	293.41	0.14	10.71	34.51	49.01	1.02
	2	230,969	370.33	410.77	0.16	8.906	31.99	43.98	1.11
C-shape	1.5	200,922	277.23	287.58	0.14	10.57	35.68	50.01	1.04
	2	231,936	347.45	377.79	0.15	8.66	32.06	43.71	1.09

Table 2 lists the material properties of steel, including Young's modulus (E), yield strength (f_y), ultimate strength (f_u), yield strain (ε_y), strain hardening strain (ε_{sh}), strain corresponding to ultimate strength (ε_u), and strain at fracture (ε_f). It can be seen from Figure 5 that compared with 1.5 mm Q235 steel, 2 mm steel has higher yield strength, but it has a shorter yield platform and lower plasticity. These material properties are also shown in Table 2. The cross sections of different sample sizes mentioned in Table 1 are geometrically calculated, and the results are listed in Table 3. Where A is the cross-sectional area; I_x and I_y are the moments of inertia around the X-axis and Y-axis, respectively; S_x is the elastic modulus around the major axis and the radius of rotation around the X-axis and Y-axis, respectively. Table 4 lists the yield strength and cross-section classification of the specimens.

Table 3. Cross-sectional properties of beam specimens.

No.	Rivet Spacing (mm)	ARHFB Sections $d_w \times b_f \times d_{f0} - d_{f1} \times t_f \times t_w$ (mm)	A (mm^2)	I_x (mm^4)	I_y (mm^4)	S_x (10^3 mm^3)	γ_x (mm)	γ_y (mm)
1	100	140 × 150 × 30 × 1.5 × 1.5	1713	9,244,783	33,361,290	92.45	73.46	139.55
2		140 × 170 × 30 × 1.5 × 1.5	1833	10,123,573	48,207,365	101.24	74.32	162.17
3		140 × 170 × 30 × 2 × 2	2432	13,346,581	64,159,426	133.47	74.08	162.42
4		140 × 170 × 40 × 1.5 × 1.5	1893	11,830,158	48,633,260	107.55	79.05	160.28
5		170 × 170 × 30 × 1.5 × 1.5	1923	14,367,883	48,207,432	124.94	86.44	158.33
6		170 × 170 × 30 × 1.5 × 2	2190	17,267,309	63,560,524	150.15	88.80	170.36
7	150	140 × 150 × 30 × 1.5 × 1.5	1713	9,244,783	33,361,290	92.45	73.46	139.55
8	200	140 × 150 × 30 × 1.5 × 1.5	1713	9,244,783	33,361,290	92.45	73.46	139.55

Table 4. Section type of rivet fastened assembled rectangular hollow flange beams (ARHFBs) with measured yield stresses.

No.	Rivet Spacing (mm)	ARHFB Sections $d_w \times b_f \times d_{f0} - d_{f1} \times t_f \times t_w$ (mm)	Flange Yield Stress (MPa)	Web Yield Stress (MPa)	Compactness		
					Flange	Web	Overall
1	100	140 × 150 × 30 × 1.5 × 1.5	277	288	S	C	S
2		140 × 170 × 30 × 1.5 × 1.5	277	288	S	C	S
3		140 × 170 × 30 × 2 × 2	347	370	S	C	S
4		140 × 170 × 40 × 1.5 × 1.5	277	288	S	C	S
5		170 × 170 × 30 × 1.5 × 1.5	277	288	S	NC	S
6		170 × 170 × 30 × 2 × 1.5	277	370	S	NC	S
7	150	140 × 150 × 30 × 1.5 × 1.5	277	288	S	C	S
8	200	140 × 150 × 30 × 1.5 × 1.5	277	288	S	C	S

Note: d_w—web depth, b_f—flange width, d_{f0}—outer flange depth, d_{f1}—inner flange depth, t_f—flange thickness, t_w—web thickness, NC—non-compact, C—compact, S—slender.

2.4. Test Setup and Measuring Equipment

The hollow flange beams (ARHFBs) connected by self-locking rivets are labeled as listed in Table 1. The test loading device is shown in Figure 7. All specimens were tested under concentrated loads of 1/4 and 3/4 to investigate the bending behavior in the pure bending section of the ARHFBs. Four-point bending tests were performed using a 100-ton hydraulic servo-machine. The loading system includes a hydraulic servo machine, a distribution beam, two loading rollers, two end rollers, as well as two support frames. Before the start of the test, a loading rate of 0.5 mm/min was used for preloading to eliminate any gap between the load and the loading system.

The preloaded load was approximately 1/10 of the bending moment bearing capacity of the beam. The applied load was loaded by displacement control. A computer was used to record the displacement during continuous loading. During loading, the force applied by the hydraulic jack was transmitted to the loading rollers through the distribution beam and finally acted on the upper flange of the ARHFBs. When the preload was repeated 5–10 times, the measurement system was returned to zero. The applied load was loaded at a rate of 1 mm/min before reaching 80% of the predicted load of the beam, and the loading rate of 0.5 mm/min was used after exceeding the predicted load. When ARHFBs produce out-of-plane buckling, the applied load begins to decrease. When the load dropped to 70% of the ultimate load of the beam, it was considered that the beam failed, and loading was stopped. During the test, the measured displacement data were recorded by the pressure-measuring elements and sensors of the hydraulic servo machine. The dynamic signal strain acquisition instrument was used to collect the strain data on the beam.

The dynamic signal strain acquisition instrument was used to collect the strain data on the beam. As shown in Figure 8, five linear displacement transducers were used to record the deflection deformation generated during the beam test. The No. 1 and No. 2 linear displacement transducers measure the compression of the upper flange of the beam.

The displacement of the pure bending section of the beam below the loading point was measured by the No. 3 and No. 5 linear displacement transducers, and the No. 4 linear displacement transducers were used to calculate the deflection deformation of the beam span. As shown in Table 5, the displacement of the upper flange compression of the beam was obtained by averaging the measured values of the No. 1 and No. 2 linear displacement transducers, and the displacement of the pure bending section below the loading point was obtained by averaging the values on the No. 3 and No. 5 linear displacement transducers.

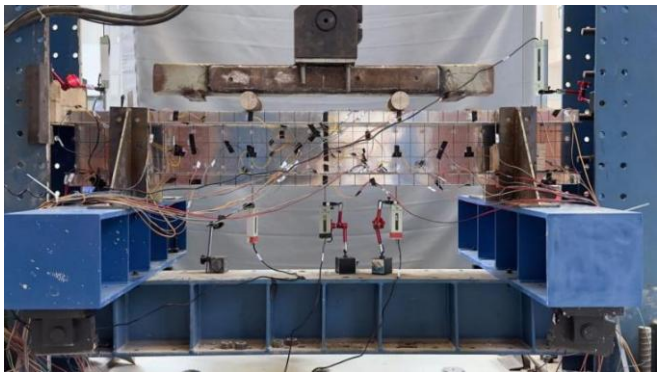

(**a**) Reality of test setup

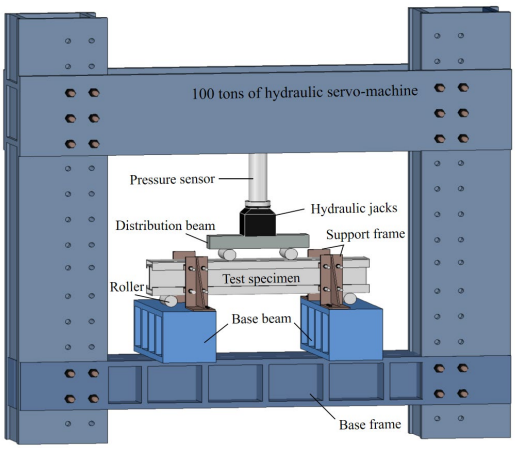

(**b**) Illustration of test setup

Figure 7. Test setup.

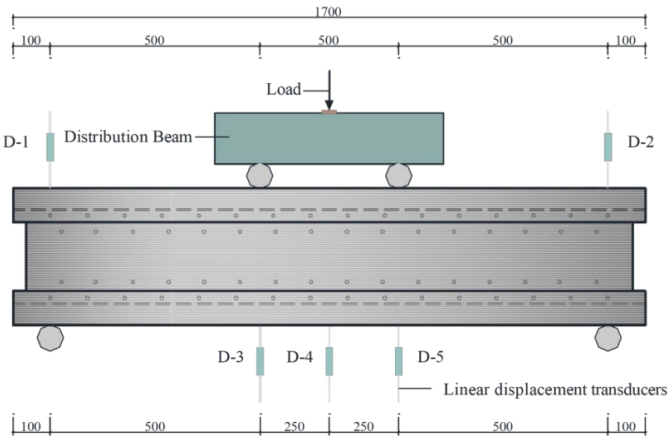

Figure 8. Displacement transducers layout diagram.

Table 5. Deformation calculation of assembled rectangular hollow flange beam (ARHFB) sections.

Calculated Position	Calculation Method of Deformation
Vertical deformation in compressed flange	$(D_1 + D_2)/2$
Vertical deformation in mid-span	(The movement of crosshead − D_4)/2
Vertical deformation in pure bending zone	$(D_3 + D_5)/2$

3. Test Results and Analysis

3.1. Test Phenomena and Failure Mode

As the applied load gradually increased during the test, all intermittently connected ARHFBs exhibited local buckling of the flange in the pure bending section, as shown in Figure 9a. With the increase in local buckling deformation of the flange, the plate separation first appeared between the adjacent rivets in the pure bending section. Then, as shown in Figure 9b, the cross-sectional heights of the left and right ends of the beam were reduced until the upper and lower surfaces of the hollow flange were in contact with each other. At this time, the web of the pure bending section of the beam underwent local buckling, and the C-shaped components underwent obvious torsional buckling, as shown in Figure 9c. This was due to the rotation of the connected points of the compressed component and the displacement of the plate in the unconnected area of the U-shaped component and the C-shaped component, so the original section shape and contour size of the components were changed. The U-shaped component that made up the hollow flange in the ARHFB limits the out-of-plane buckling of the C-shaped component that made up the lower surface of the flange. The out-of-plane deformation of the U-shaped component was suppressed by the lateral support frames in the loading system. The plate separation between adjacent rivets under the pure bending section of the ARHFB reached the maximum (Figure 9d), and this phenomenon gradually spread from the center of the pure bending section to the left and right ends of the beam with the pure bending section as the center. The corrugated deformation appeared in the left and right webs below the loading point of the ARHFB (Figure 9e), and the obvious deflection appeared in the lower flange (Figure 9f) until the beam was damaged.

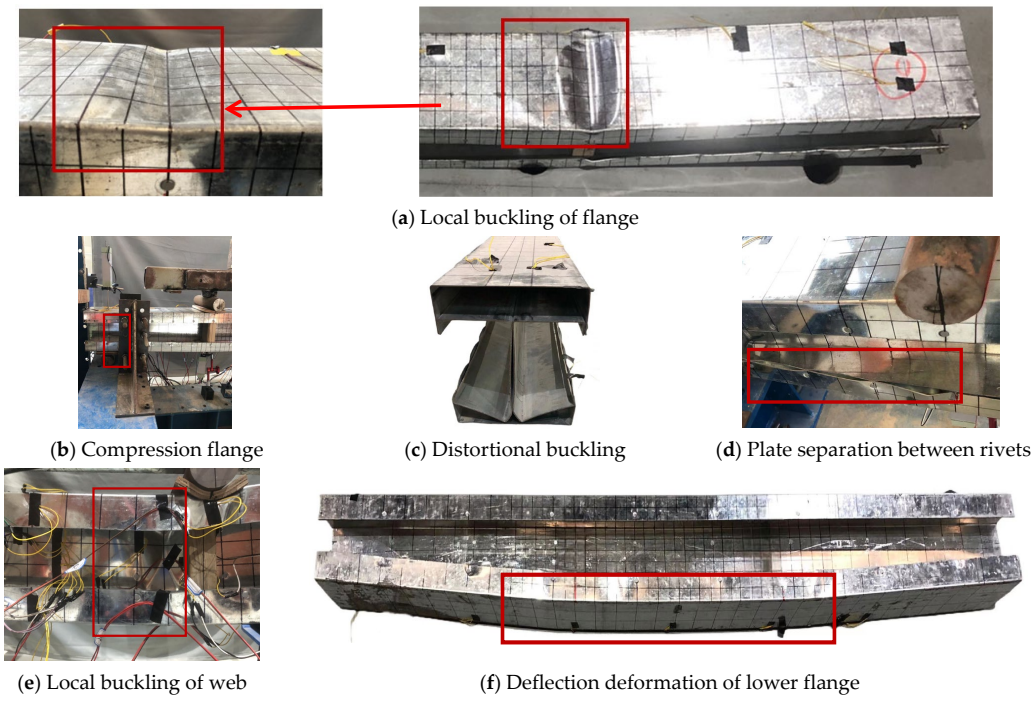

(**a**) Local buckling of flange

(**b**) Compression flange (**c**) Distortional buckling (**d**) Plate separation between rivets

(**e**) Local buckling of web (**f**) Deflection deformation of lower flange

Figure 9. Typical failure modes of assembled rectangular hollow flange beam (ARHFB) specimens under four-point loading conditions.

3.2. Test Data Analysis

The load–displacement curves of all specimens are shown in Figure 10. Table 5 shows the calculation method of displacement at each position. For all ARHFB specimens, the load–displacement curve can be divided into three stages. In the first stage, the increase of vertical displacement is small because the specimen remains elastic. At this time, the displacement of the sample changes linearly with the increase of the load, and there is a slight plate separation between the rivets of the pure bending section of the specimen. In the second stage, the overall height of the specimen is reduced by being continuously compressed. Since the continuous increase of vertical displacement and no significant change of load, it is shown as a platform-like segment on the curve. According to Figure 10, the ARHFB cross-section exhibits weak cyclic behavior. From Figure 10d,f, it can be seen that the increase in flange depth and web depth leads to an increase in the total depth d of the design section; meanwhile, the platform section will also be lengthened. From the slope of the curve, it can be seen that after the upper flange begins to buckle until the inner surfaces of the upper and lower flanges are in contact with each other, the bending stiffness increases rapidly through the platform segment. When the cavity of the hollow flange is completely compressed, the curve enters the third stage. At this time, as the displacement increases, the load rises rapidly until failure.

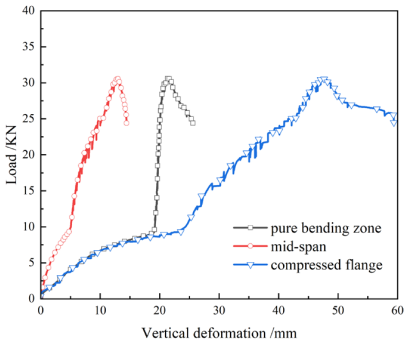

(**a**) 140 × 150 × 30 × 1.5 × 1.5 − 100

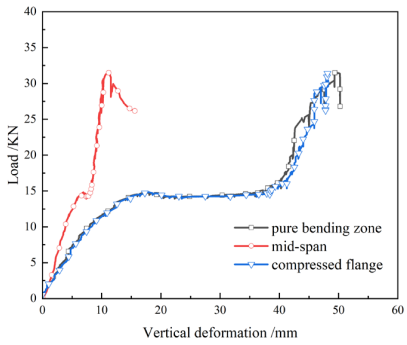

(**b**) 140 × 170 × 30 × 1.5 × 1.5

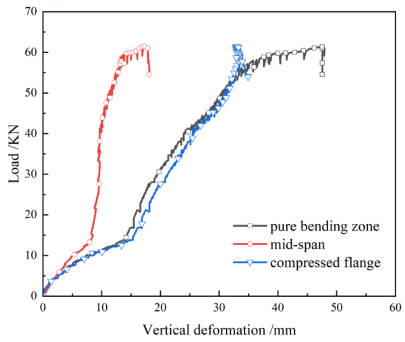

(**c**) 140 × 170 × 30 × 2 × 2

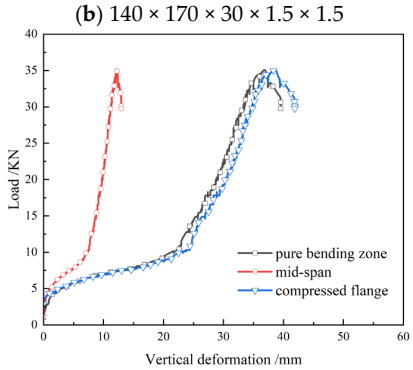

(**d**) 140 × 170 × 40 × 1.5 × 1.5

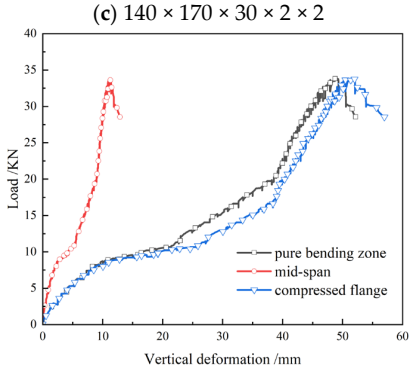

(**e**) 170 × 170 × 30 × 1.5 × 1.5

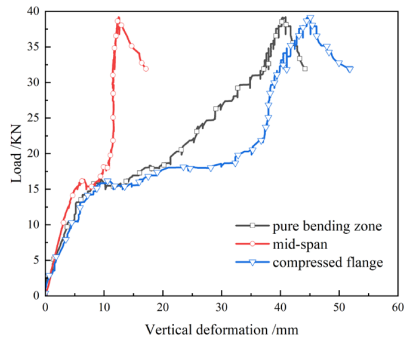

(**f**) 170 × 170 × 30 × 1.5 × 2

Figure 10. *Cont.*

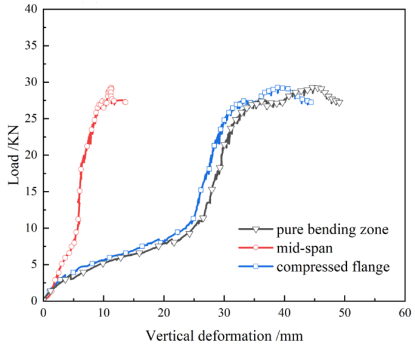

(**g**) 140 × 150 × 30 × 1.5 × 1.5 − 150

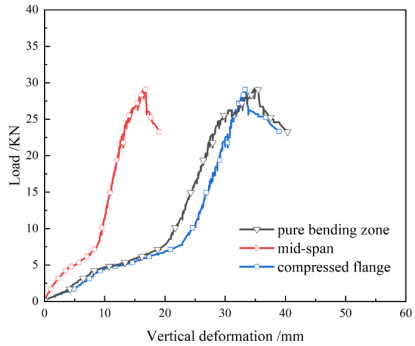

(**h**) 140 × 150 × 30 × 1.5 × 1.5 − 200

Figure 10. Curves of load vertical deflection.

Comparing Figure 10a,g,h, it can be seen that with the rivet spacing increasing from 100 mm to 150 mm and 200 mm, the ultimate bearing capacity of the specimen decreased by 3.23% and 4.20%, respectively. According to Figure 10a,b, the flange width is increased by 20 mm from 150 mm to 170 mm, and the bearing capacity is only increased by 2.9%. Increasing the total depth of the section mainly depends on increasing the depth of the flange and the depth of the web, which will lead to an increase in the bearing capacity of the specimen. According to Figure 10b,e, the web depth is increased by 30 mm from 140 mm to 170 mm, and the bearing capacity is increased by 6%. According to Figure 10b,d, the flange depth grows by 10 mm from 30 mm to 40 mm, and the bearing capacity is increased by 8%. The above shows that increasing the flange depth is a more effective way to improve the bearing capacity of the ARHFBs. In Figure 10b,c, it can be seen that the thickness of steel increases from 1.5 mm to 2 mm, and the bearing capacity increases by 95%. Increasing the thickness of steel is a method that can greatly improve the bearing capacity of the section. When only the thickness of the web thickness is increased, as shown in Figure 10e,f, the bearing capacity of the specimen is increased by 25%. This shows that thicker webs are recommended in engineering practice.

4. Numerical Analyses

4.1. Development of Numerical Models

In this paper, ABAQUS 2020 [19] is used for finite element simulation to study the bending resistance and strength of ARHFB under a concentrated load at 1/4 and 3/4 points. All ARHFBs in this study are modeled using the S4R element type with simplified integration and limited membrane strain. The loading roller in the test is modeled by an R3D4 four-node three-cone bilinear rigid quadrilateral. This method has been proven to be able to simulate the buckling behavior of beams and has been successfully used in many studies [20–24]. The steel properties are determined according to the data obtained from the tensile test. The nominal strain–nominal stress curve measured by the test is transformed into real stress–real strain so as to obtain the real stress–effective plastic strain curve of the material. This study uses a bilinear stress–strain model simplified by the real stress–effective plastic strain curve, in which the strain-hardening part is ignored.

In this study, the specimen grid is 14 mm × 14 mm, and the loading roller adopts a 10 mm × 10 mm grid to obtain more accurate calculation results. Two models, including the half-span model and the full-length model, are established simultaneously, and the calculation accuracy and calculation time of the two models are compared. Finally, the half-span symmetric model is adopted in this paper to reduce the calculation time as much as possible on the premise of ensuring the accuracy of the model. Due to the symmetry of the loading system, the half-span model adopts symmetrical boundary conditions (3,4,5) at the mid-span position, and the other end still limits the displacement in the X and Y directions and the rotation in the Z direction (1,2,6). This allows the longitudinal displacement of the beam in the Z direction and the vertical displacement in the Y direction to be allowed. This simulates the experimental conditions in which only one end allows Z-axis translation in

the actual test. In the numerical simulation, two analysis methods are mainly used: elastic buckling and nonlinear buckling. The buckling mode and critical buckling moment (M_{ol}) of each specimen are obtained by elastic buckling. The initial geometric imperfections obtained in the elastic buckling analysis are introduced into the nonlinear buckling analysis. The numerical models established in the simulation are shown in Figure 11. Xue et al. [24] provided the specific modeling process of ARHFBs.

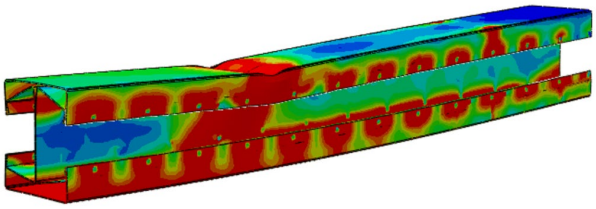

(**a**) full-length model

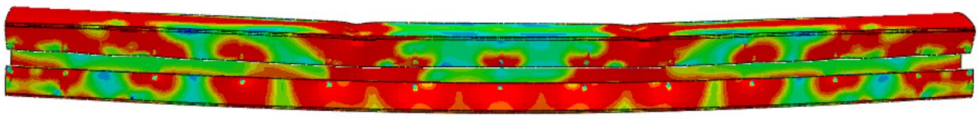

(**b**) half-length model

Figure 11. Finite element analysis results of the specimen.

4.2. Verification of FEM

The developed finite element model was verified by comparing the four-point bending test results with the finite element simulation results to ensure the validity of the finite element model. Figure 11 records the failure modes of the full-length model and the half-span model, respectively. Comparing it with the failure mode of the ARHFB in the pure bending state obtained from the experiment in Figure 9, it can be seen that the finite element simulation results are in good agreement with the experimental results. In order to further ensure the accuracy of the follow-up study, the specimen 140 × 150 × 30 × 1.5 × 1.5—100 was taken as an example to compare its finite element analysis curve with the curve obtained from the test, as shown in Figure 12. It can be seen that the overall trend of the two curves is consistent. The finite element analysis simulates the whole process of the test well, and the developed finite element model is verified. The test and simulation results of eight specimens are recorded in Tables 6 and 7. The average value of the ratio of test results to simulation results is 0.99, and the COV value is 0.03. The error is basically kept within 6%. This verifies the applicability of the shell element, mesh density, contact, boundary conditions, and model materials in the finite element and shows that the finite element model can better simulate the stress state of the model structure.

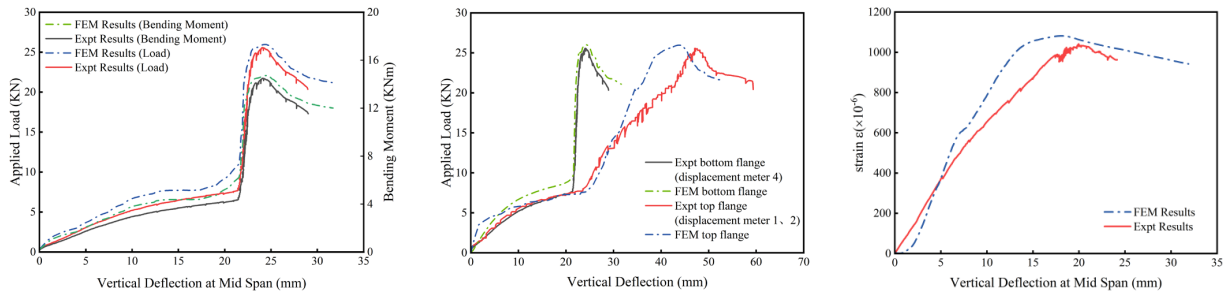

(**a**) (**b**) (**c**)

Figure 12. Experimental and finite element results for 140 × 150 × 30 × 1.5 × 1.5 assembled rectangular hollow flange beam (ARHFB).

Table 6. Comparison of the experimental ultimate bending moment with the finite element ultimate bending moment.

No.	Rivet Spacing (mm)	ARHFB Sections $d_w \times b_f \times d_{f0} - d_{f1} \times t_f \times t_w$ (mm)	Test M_u (kN·m)	FEA M_u (kN·m)	$M_{u,Test}/M_{u,FEA}$
1	100	140 × 150 × 30 × 1.5 × 1.5	17.35	17.52	0.99
2		140 × 170 × 30 × 1.5 × 1.5	17.86	18.20	0.98
3		140 × 170 × 30 × 2 × 2	34.89	35.12	0.99
4		140 × 170 × 40 × 1.5 × 1.5	19.29	18.67	1.03
5		170 × 170 × 30 × 1.5 × 1.5	18.45	17.57	1.05
6		170 × 170 × 30 × 1.5 × 2	22.32	23.70	0.94
7	150	140 × 150 × 30 × 1.5 × 1.5	16.79	17.36	0.97
8	200	140 × 150 × 30 × 1.5 × 1.5	16.62	16.98	0.98
Mean		0.99			
Cov		0.03			

4.3. Parametric Studies

Based on the finite element model, which is in good agreement with the test results, a series of parameter analyses were carried out. The buckling behavior of rivet-fastened ARHFBs under four-point bending was further studied. These sections with different rivet spacing, span, web depth, steel thickness, and steel grade were studied. Table 8 analyzes the three main parameters (rivet spacing, span, web depths) of ARHFBs composed of the same steel grade Q235. The rivet spacing is 0 mm, 100 mm, 150 mm, and 200 mm; among them, the 0 mm rivet spacing was used to simulate the welding ARHFBs. Four different spans of 1700 mm, 2300 mm, 2700 mm, and 3300 mm were selected. Three web depths were 140 mm, 180 mm, and 200 mm. Table 9 studies the bearing capacity of ARHFBs with rivet spacing of 100 mm under different plate thicknesses and steel grades. Based on the experimental study, the web thickness has a greater influence on the bearing capacity of ARHFBs than the flange thickness. Two different flange thicknesses (1.5 mm and 2 mm) and three different web thicknesses (1.5 mm, 2 mm and 3 mm) were used. Two different steel grades, Q235 and Q345, were selected to study the bearing capacity of ARHFBs composed of webs and flanges with different steel grades.

Table 7. Test results and comparison with the predicted results of GB50018.

Test No.	Rivet Spacing (mm)	ARHFBs Sections $d_w \times b_f \times d_{f0} - d_{f1} \times t_f \times t_w$ (mm)	S_x (10^3 mm^3)	M_y (kN·m)	M_u (kN·m)		GB50018		
					Test	FEM	M_S (kN·m)	$M_{u,FEM}/M_S$	$M_{u,Test}/M_S$
1	100	140 × 150 × 30 × 1.5 × 1.5	92.45	26.28	17.35	17.52	17.72	0.99	0.98
2		140 × 170 × 30 × 1.5 × 1.5	101.24	28.78	17.86	18.20	20.54	0.89	0.87
3		140 × 170 × 30 × 2 × 2	133.47	48.35	34.89	35.12	31.98	1.10	1.09
4		140 × 170 × 40 × 1.5 × 1.5	107.55	30.63	19.29	18.67	23.88	0.78	0.81
5		170 × 170 × 30 × 1.5 × 1.5	124.94	35.47	18.45	17.57	19.08	0.92	0.97
6		170 × 170 × 30 × 1.5 × 2	150.15	51.26	22.32	23.70	34.32	0.69	0.65
7	150	140 × 150 × 30 × 1.5 × 1.5	92.45	26.28	16.79	17.36	17.72	0.98	0.95
8	200	140 × 150 × 30 × 1.5 × 1.5	92.45	26.28	16.62	16.98	17.72	0.96	0.94

Note: S_x—elastic section modulus, M_y—first yield moment, M_u—ultimate moment, M_s—section moment capacity.

The finite element model used in the parametric analysis has the same element type, contact, and boundary conditions as the verified finite element model. The material properties are adopted according to specification GB50017-2017 [25]. The elastic modulus is 2.06×10^5 MPA, and the Poisson's ratio is 0.3. The yield strength of the Q235 steel grade is 235 MPa, and the ultimate strength is 370 MPa. The yield strength of the Q345 steel grade is 345 MPa, and the ultimate strength is 470 MPa. The initial defect is L/1000. The next section will introduce and analyze the finite element results.

Table 8. Results of the parametric study and comparison with predicted results of AISI S100-16 and GB50018—Q235 steel grade assembled rectangular hollow flange beams (ARHFBs).

Rivet Spacing (mm)	ARHFB Sections $d_w \times b_f \times d_{f0} - d_{f1} \times t_f \times t_w$ (mm)	L (mm)	Compactness		Z (10^3 mm^3)	M_y (kN·m)	M_{ol} (kN·m)	$M_{u,FEA}$ (kN·m)	λ_l	AISI S100				GB50018	
										EWM			DSM		
			Flange	Web						Z_e (10^3 mm^3)	M_s (kN·m)	$M_{u,FEA}/M_S$	M_u/M_y	M_S (kN·m)	$M_{u,FEA}/M_S$
0	140 × 150 × 30 × 1.5 × 1.5	1700	S	C	92.45	21.73	21.94	15.86	1.00	70.04	16.46	0.96	0.73	14.66	1.08
	180 × 150 × 30 × 1.5 × 1.5	1700	S	NC	122.01	28.67	29.53	16.91	0.99	92.54	21.75	0.78	0.59	19.75	0.86
	200 × 150 × 30 × 1.5 × 1.5	1700	S	NC	137.54	32.32	33.47	17.13	0.98	104.54	24.57	0.70	0.53	22.46	0.76
	140 × 150 × 30 × 1.5 × 1.5	2300	S	C	92.45	21.73	20.61	15.79	1.03	70.04	16.46	0.96	0.73	14.66	1.08
	140 × 150 × 30 × 1.5 × 1.5	2700	S	C	92.45	21.73	20.32	14.52	1.03	70.04	16.46	0.88	0.67	14.66	0.99
	140 × 150 × 30 × 1.5 × 1.5	3300	S	C	92.45	21.73	20.15	13.34	1.04	70.04	16.46	0.81	0.61	14.66	0.91
100	140 × 150 × 30 × 1.5 × 1.5	1700	S	C	92.45	21.73	20.56	15.50	1.03	70.04	16.46	0.94	0.71	14.66	1.00
	180 × 150 × 30 × 1.5 × 1.5	1700	S	C	92.45	28.67	27.63	16.14	0.89	92.54	21.75	0.74	0.74	19.75	1.10
	200 × 150 × 30 × 1.5 × 1.5	1700	S	C	92.45	32.32	29.79	16.82	0.85	104.54	24.57	0.68	0.77	22.46	1.15
	140 × 150 × 30 × 1.5 × 1.5	2300	S	C	92.45	21.73	20.43	14.65	1.03	70.04	16.46	0.89	0.67	14.66	1.06
	140 × 150 × 30 × 1.5 × 1.5	2700	S	C	92.45	21.73	20.07	14.37	1.04	70.04	16.46	0.87	0.66	14.66	0.98
	140 × 150 × 30 × 1.5 × 1.5	3300	S	C	92.45	21.73	19.74	13.03	1.05	70.04	16.46	0.79	0.60	14.66	0.89
150	140 × 150 × 30 × 1.5 × 1.5	1700	S	C	92.45	21.73	20.47	14.45	1.03	70.04	16.46	0.88	0.67	14.66	0.92
	180 × 150 × 30 × 1.5 × 1.5	1700	S	NC	122.01	28.67	27.59	14.97	1.02	92.54	21.75	0.69	0.52	19.75	0.76
	200 × 150 × 30 × 1.5 × 1.5	1700	S	NC	137.54	32.32	29.68	15.81	1.04	104.54	24.57	0.64	0.49	22.46	0.70
	140 × 150 × 30 × 1.5 × 1.5	2300	S	C	92.45	21.73	19.92	13.47	1.04	70.04	16.46	0.82	0.62	14.66	0.99
	140 × 150 × 30 × 1.5 × 1.5	2700	S	C	92.45	21.73	18.82	13.02	1.07	70.04	16.46	0.79	0.60	14.66	0.89
	140 × 150 × 30 × 1.5 × 1.5	3300	S	C	92.45	21.73	16.37	11.91	1.08	70.04	16.46	0.72	0.55	14.66	0.81
200	140 × 150 × 30 × 1.5 × 1.5	1700	S	C	92.45	21.73	20.32	12.92	1.03	70.04	16.46	0.78	0.59	14.66	0.83
	180 × 150 × 30 × 1.5 × 1.5	1700	S	NC	122.01	28.67	27.54	13.21	1.02	92.54	21.75	0.61	0.46	19.75	0.67
	200 × 150 × 30 × 1.5 × 1.5	1700	S	NC	137.54	32.32	29.46	13.78	1.04	104.54	24.57	0.56	0.43	22.46	0.61
	140 × 150 × 30 × 1.5 × 1.5	2300	S	C	92.45	21.73	19.48	12.15	1.06	70.04	16.46	0.74	0.56	14.66	0.88
	140 × 150 × 30 × 1.5 × 1.5	2700	S	C	92.45	21.73	17.04	11.38	1.07	70.04	16.46	0.69	0.52	14.66	0.78
	140 × 150 × 30 × 1.5 × 1.5	3300	S	C	92.45	21.73	14.36	9.43	1.08	70.04	16.46	0.57	0.43	14.66	0.64

Table 9. Results of the parametric study and comparison with predicted results of AISI S100-16 and GB50018—100 mm rivet spacing assembled rectangular hollow flange beams (ARHFBs).

ARHFB Sections $d_w \times b_f \times d_{f0} - d_{f1} \times t_f \times t_w$ (mm)	L (mm)	Compactness		Steel Grade (Mpa)		Z (10^3 mm^3)	M_y (kN·m)	M_{ol} (kN·m)	$M_{u,FEA}$ (kN·m)	λ_l	AISI S100				GB50018	
											EWM			DSM		
		Flange	Web	U-Shape Component	C-Shape Component						Z_e (10^3 mm^3)	M_s (kN·m)	$M_{u,FEA}/M_S$	M_u/M_y	M_S (kN·m)	$M_{u,FEA}/M_S$
140 × 150 × 30 × 1.5 × 1.5	1700	S	NC	235	345	92.45	25.19	25.63	20.08	0.99	67.95	18.63	1.08	0.80	17.04	1.18
140 × 150 × 30 × 1.5 × 1.5	1700	S	C	345	235	92.45	28.43	23.91	16.92	1.09	61.90	18.46	0.92	0.60	19.13	0.88
140 × 150 × 30 × 1.5 × 1.5	1700	S	C	235	235	92.45	21.73	20.56	14.65	1.03	70.04	16.46	0.89	0.67	14.66	1.00
140 × 150 × 30 × 1.5 × 1.5	1700	S	NC	345	345	92.45	31.89	26.27	21.42	1.10	59.81	20.63	1.04	0.67	21.52	1.00
140 × 150 × 30 × 1.5 × 2	1700	S	C	235	345	102.37	28.62	27.93	28.53	1.01	75.53	21.25	1.34	1.00	19.37	1.47
140 × 150 × 30 × 1.5 × 2	1700	S	C	345	235	102.37	30.76	25.80	22.68	1.09	70.15	20.40	1.11	0.74	20.72	1.09
140 × 150 × 30 × 1.5 × 2	1700	S	C	235	235	102.37	24.06	23.37	21.56	1.01	78.29	18.40	1.17	0.90	16.24	1.33
140 × 150 × 30 × 1.5 × 2	1700	S	C	345	345	102.37	35.32	28.44	30.02	1.11	67.38	23.25	1.29	0.85	23.84	1.26
140 × 150 × 30 × 1.5 × 3	1700	S	C	235	345	121.40	35.18	51.25	49.04	0.83	89.94	26.22	1.87	1.39	23.78	2.06
140 × 150 × 30 × 1.5 × 3	1700	S	C	345	235	121.40	35.23	38.14	36.85	0.96	85.89	24.10	1.53	1.05	23.72	1.55
140 × 150 × 30 × 1.5 × 3	1700	S	C	235	235	121.40	28.53	34.73	35.68	0.91	94.04	22.10	1.61	1.25	19.25	1.85
140 × 150 × 30 × 1.5 × 3	1700	S	C	345	345	121.40	41.88	50.76	50.08	0.91	81.80	28.22	1.77	1.20	28.26	1.77
140 × 150 × 30 × 2 × 1.5	1700	S	NC	235	345	111.94	29.75	26.31	22.94	1.06	81.84	21.88	1.05	0.77	20.07	1.14
140 × 150 × 30 × 2 × 1.5	1700	S	C	345	235	111.94	35.17	21.88	18.11	1.27	73.10	22.34	0.81	0.51	23.61	0.77
140 × 150 × 30 × 2 × 1.5	1700	S	C	235	235	111.94	26.30	19.30	16.90	1.17	83.93	19.72	0.86	0.64	17.70	0.95
140 × 150 × 30 × 2 × 1.5	1700	S	NC	345	345	111.94	38.62	26.73	24.15	1.20	71.01	24.50	0.99	0.63	25.98	0.93
140 × 150 × 30 × 2 × 2	1700	S	C	235	345	121.82	33.16	33.72	31.93	0.99	89.37	24.48	1.30	0.96	22.39	1.43
140 × 150 × 30 × 2 × 2	1700	S	C	345	235	121.82	37.49	27.31	26.75	1.17	81.31	24.27	1.10	0.71	25.19	1.06
140 × 150 × 30 × 2 × 2	1700	S	C	235	235	121.82	28.63	25.86	25.27	1.05	92.13	21.65	1.17	0.88	19.28	1.31
140 × 150 × 30 × 2 × 2	1700	S	C	345	345	121.82	42.03	35.54	35.46	1.09	78.54	27.10	1.31	0.84	28.30	1.25

4.4. Bearing Capacity Comparison of Different Types of ARHFBs

In Figure 13a,b, we compare the ultimate moments of the ARHFBs with different spans and web depths using the Q235 steel grade. In Figure 13a, the data points of the ARHFBs with different rivet spacing (0 mm, 100 mm, 150 mm, 200 mm) under different spans have the same trend. That is, the bearing capacity decreases with the increase in rivet spacing. When the rivet spacing is 0 mm, it is considered welded. When the rivet spacing is 100 mm, the bearing capacity is the closest to that of welding; the maximum difference is only 3%. When the rivet spacing is 150 mm and 200 mm, the bearing capacity of the specimen decreases rapidly; the minimum decrease values are 10% and 18%, respectively. In this case, the rivet-fastened connection method can no longer replace the welding connection method. When the span of ARHFBs ranges from 1700 mm to 3300 mm, the bearing capacity of the specimen decreases with the increase in span. The span of ARHFBs doubled, while the bearing capacity decreased by only 15%. ARHFBs will not decrease significantly with the increase in span, which makes ARHFBs more suitable for use in large-span buildings. Figure 13b draws the bearing capacity of ARHFBs with different web depths under different rivet spacing in a similar way. When the web is increased from 140 mm to 180 mm, the increase in rivet spacing leads to an average reduction in bearing capacity by 8%. When the web is increased from 180 mm to 200 mm, the bearing capacity is reduced by 6% on average. It can be seen that when the depth of the web increases, the reduction in the bearing capacity caused by the increase in rivet spacing is weakened. This shows the importance of web depth on the bearing capacity of ARHFBs.

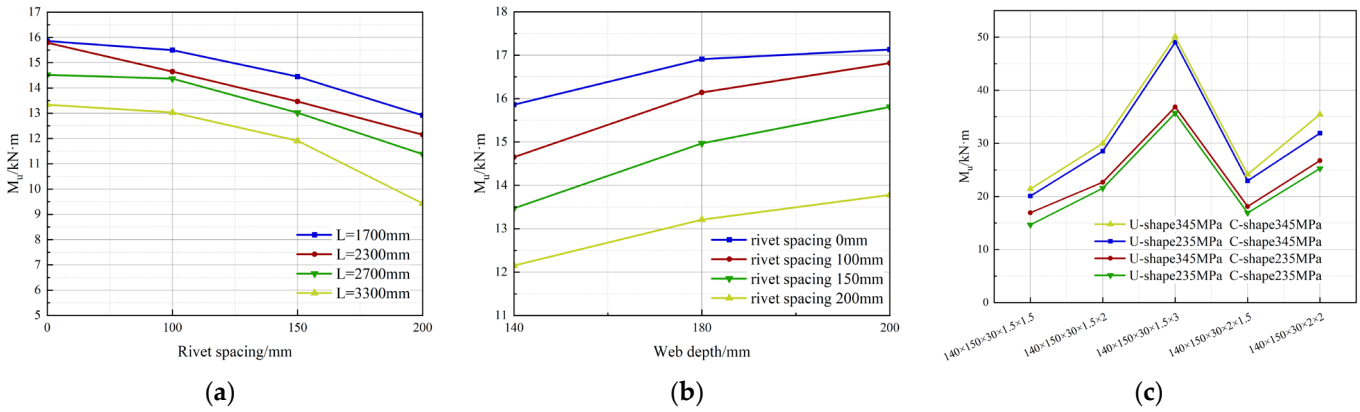

Figure 13. The influence of several parameters.

To determine which parameter among web and flange strength is more important for the loading capacity of the ARHFBs, the loading capacity of ARHFBs with different web and flange strengths under the same thickness is studied, as shown in Figure 13c. It is clear that with the increase in web and flange strength, the overall bearing capacity of the specimen also increased. From Figure 13c, the data points of 'U-shape 235 MPa C-shape 345 MPa' are higher than the data points of 'U-shape 235 MPa C-shape 235 MPa'. The difference between the data points of 'U-shape 235 MPa C-shape 235 MPa' and 'U-shape 345 MPa C-shape 235 MPa' is small; the maximum is only 9%. Under the premise of the same strength of C-shaped components (web), increasing the strength of U-shaped components (flange), the bearing capacity changes little, and the maximum increase is only 15%. However, under the premise of the same strength of U-shaped components, increasing the strength of C-shaped components will significantly improve the bearing capacity by at least 37%. This indicates that the web strength of the ARHFBs is a more important parameter. Figure 13c also compares the loading capacity of ARHFBs with different flange and web thicknesses. The bearing capacity difference between the specimen '140 × 150 × 30 × 2 × 1.5' and the specimen '140 × 150 × 30 × 2 × 2' is 39%. The bearing capacity difference between the specimen '140 × 150 × 30 × 1.5 × 2' and the specimen '140 × 150 × 30 × 2 × 2' is only 10%. When the flange thickness is 2 mm, the web increases from 1.5 mm to 2 mm, and

the bearing capacity is increased by 39%. While the web thickness remains unchanged at 2 mm, the flange thickness increases from 1.5 mm to 2 mm, and the bearing capacity only increases by 10%. Increasing the thickness of either the flange or the web will improve the overall bearing capacity of the specimen. However, the improvement of the bearing capacity caused by increasing the flange thickness is more obvious.

5. Comparison with Design Codes

In order to select a more accurate design method to predict the bearing capacity of the riveting connection ARHFBs, existing design methods of cold-formed thin-walled steel beams are evaluated according to the bearing capacity of ARHFBs obtained by experiments and parametric studies. The results from the test and finite element analysis results are compared with the current design standards of cold-formed steel structures in the United States and China, GB50018 [16] and AISI S100-2016 [17], respectively. The comparison between the experimental values and the two specifications is shown in Tables 6 and 7. Tables 8 and 9 show the calculation results in the parameter study under the two specifications.

5.1. GB50018-2002 Technical Code for Cold-Formed Thin-Walled Steel Structures

In this section, the GB50018 Technical Code for Cold-Formed Thin-Walled Steel Structures [16] is used to predict the bending capacity of ARHFB. According to Formula (1) given in Article 5.3.1 of GB50018-2002 [16], the bearing capacity of the flexural component with load passing through the bending center and parallel to the major axis is calculated, where W_{enx} is the smaller effective net section modulus of the major axis, and f_y is the yield strength. For the flexural composite steel components connected by rivets, the design value of the tensile bearing capacity of the connectors is calculated using the provisions of Article 6.1.8-3 of GB50018 [16].

$$\sigma = \frac{M_{max}}{W_{enx}} \leq f \tag{1}$$

According to Table 7, the maximum difference in the prediction of the ARHFBs of the experimental study is 35%, and the minimum difference is 1%. According to Table 9, the predicted results are close to the actual measured values for different strength grades and thicknesses. This is because the calculation default in GB50018 adopts the same type of steel grades without considering the difference between the flange and web of different yield strengths in the mixed section. For mixed sections with different web and flange thicknesses, GB500018 often overestimates its bearing capacity. It can be seen from Table 8 that the maximum difference in the prediction of the bearing capacity of the specimens using Q235 steel in the parameter study is 39%, and the minimum difference is 1%. The prediction ability of GB50018 for ARHFB decreases with the increase in rivet spacing. This is because GB50018 only gives a calculation formula for the design value of the tensile bearing capacity of the connector without considering the influence of the rivet group on the bending moment bearing capacity of the section. When the rivet spacing is 0 mm, the loading capacity of the specimen under welding is simulated. Therefore, GB50018 can conservatively estimate ARHFBs with rivet spacing of 0 mm, as proposed in this paper. As an alternative connection method for welding, the loading capacity of 100 mm rivet spacing can also be well predicted.

5.2. AISI S100-2016—North American Specification for the Design of Cold-Formed Steel Structural Members

This section evaluates the load-carrying capacity of ARHFBs using specifications developed by the American Iron and Steel Institute (AISI). The AISI S100 specification focuses on providing accurate information on the design of cold-formed steel. The code was developed with reference to codes and standards in the United States, Mexico, and Canada. Based on the previously mentioned damage modes of ARHFBs, the AISI code section on local buckling and yielding and overall buckling interaction was chosen to be used. The F3 local buckling and yielding and overall buckling interaction section of AISI consists of

two main calculation methods, the effective width method and the direct strength method. Since none of the ARHFB members are open in this paper, the equations in F3.1.1 and F3.2.1 were chosen to predict and evaluate the flexural capacity of the ARHFBs.

5.2.1. Effective Width Method (EWM)

In AISI S100, the effective section modulus Z_e is calculated separately for each member based on the effective width. AISI S100 specification F3.1.1 specifies that the width b of a member is the width of the plane, excluding the radius of cold bending on both sides. The effective width (b_e) of a uniformly compressed member is calculated separately according to Equations (2) and (3) to obtain the effective section modulus of the specimen as a whole. The prediction of the load-carrying capacity of a specimen using the effective width method in AISI S100 is the same as the formula recommended in AN/NZS 4600.

$$\text{For } \lambda \leq 0.673 \; b_e = b \tag{2}$$

$$\text{For } \lambda > 0.673 \; b_e = \rho b \tag{3}$$

The effective width is chosen based on the size of the aspect ratio λ. The length-to-finish ratio λ is calculated according to Equation (4). Where f^* is the design stress of the compression member calculated based on the effective design width and f_{cr} is the elastic buckling stress. It is worth mentioning that the buckling coefficient K is introduced in the elastic buckling stress of the member. K is the member supported by the web on each longitudinal edge, which is taken as 4. When $\lambda > 0.673$, the effective width factor ρ is introduced. The effective width coefficient ρ is calculated using Equation (6).

$$\lambda = \sqrt{\frac{f^*}{f_{cr}}} \tag{4}$$

$$f_{cr} = \left(\frac{k\pi^2 E}{12(1-\nu^2)}\right)\left(\frac{t}{b}\right)^2 \tag{5}$$

$$\rho = \frac{\left(1 - \frac{0.22}{\lambda}\right)}{\lambda} \leq 1.0 \tag{6}$$

Table 10 records the cross-section moment load capacity of the ARHFB in the test calculated using the above equation, and the obtained values are compared with the results of the test study and finite element simulation results. According to the comparison results, the effective width method proposed in AISI S100 can predict the ARHFBs with different rivet spacing better with a maximum difference of only 9% when the rivet spacing of "140 × 150 × 30 × 1.5 × 1.5" ARHFBs are 100 mm, 150 mm, and 200 mm. However, since the calculation formula does not involve the load-bearing capacity reduction factor brought about by the relevant rivet spacing, the existing sample size can not be fully determined by the specification for the prediction of the load-bearing capacity of ARHFBs with different rivet spacing. For ARHFBs with 100 mm rivet spacing, the predictions of EWM are more accurate for flange widths ranging from 150 mm to 170 mm.

Table 10. Test results and comparison with the predicted results of AISI S100-2016.

Test No.	Rivet Spacing (mm)	ARHFBs Sections $d_w \times b_f \times d_{f0} - d_{f1} \times t_f \times t_w$ (mm)	Z_e (10^3 mm^3)	M_y (kN·m)	M_u (kN·m)		AISI S100-EWM		
					Test	FEM	M_s (kN·m)	$M_{u,Test}/M_S$	$M_{u,FEA}/M_S$
1	100	140 × 150 × 30 × 1.5 × 1.5	64.45	26.28	17.35	17.52	18.28	0.95	0.96
2		140 × 170 × 30 × 1.5 × 1.5	65.72	28.78	17.86	18.20	18.64	0.96	0.98
3		140 × 170 × 30 × 2 × 2	78.15	48.35	34.89	35.12	28.17	1.24	1.25
4		140 × 170 × 40 × 1.5 × 1.5	65.59	30.63	19.29	18.67	18.63	1.04	1.00
5		170 × 170 × 30 × 1.5 × 1.5	82.13	35.47	18.45	17.57	23.26	0.79	0.76
6		170 × 170 × 30 × 1.5 × 2	90.03	51.26	22.32	23.70	30.02	0.74	0.79
7	150	140 × 150 × 30 × 1.5 × 1.5	64.45	26.28	16.79	17.36	18.28	0.92	0.95
8	200	140 × 150 × 30 × 1.5 × 1.5	64.45	26.28	16.62	16.98	18.28	0.91	0.93

Note: Z_e—elastic section modulus, M_y—first yield moment, M_u—ultimate moment, M_s—section moment capacity.

The larger the flange width of the test specimen, the more accurate the prediction of the load-carrying capacity by EWM. When the web height is raised from 140 mm to 170 mm, the difference in the prediction of ARHFB load carrying capacity by EWM widens from 0.78 KN to 4.81 KN, with a maximum difference of 21%. This may be due to the fact that the effective widths of the two members are not calculated separately in the EWM, and the pieced hollow flange shape for the ARHFB makes the boundary conditions of the lip of the C-shaped member constrained. Based on the prediction results of EWM for ARHFBs with different thicknesses in Table 10, it can be seen that EWM is less capable of predicting ARHFBs for mixed sections with webs and flanges with different strengths. Meanwhile, for ARHFBs with the same thickness of the flange and web, the increase in thickness decreases the predictive ability of EWM.

To further explore the predictive ability of EWM for ARHFBs, the ARHFB used in the parameter study was calculated. In the parameter study, the prediction ability of EWM for ARHFBs with a steel grade of Q235 decreases with the increase in rivet spacing. Because the calculation formula of EWM does not consider the decrease in bearing capacity caused by the span of the specimen, the prediction ability of EWM gradually decreases with the increase of span. As the height of the web increases from 140 mm to 200 mm, the stability of the prediction of EWM of the bearing capacity of the ARHFBs gradually decreases. This is consistent with the results obtained by comparing the test specimens. In the parameter study, ARHFBs with rivet spacing of 100 mm have a better prediction ability than ARHFBs with uniform overall strength. The ARHFB with thickness from 1.5 mm to 2 mm predicted by EWM has a maximum difference of 31% with the finite element simulation results. When the thickness of steel increases, the prediction of EWM often underestimates the bearing capacity of ARHFBs. For mixed sections with different thicknesses of webs and flanges, the underestimation of the bearing capacity of ARHFBs becomes more and more obvious. It is suggested that the calculation method of the effective width of U-shaped members should be modified to obtain more accurate prediction results.

5.2.2. Direct Strength Method (DSM)

In AISI S100, for the direct strength method, calculations are performed according to sections F3.2.1-F3.2.3 of the specification. Compared to AS/NZS 4600, the local inelastic reserve capacity of the specimen is considered in section F3.2.3 of the AISI specification. However, it presupposes $\lambda_l \leq 0.776$ and $M_{ne} \geq M_y$. Therefore, the formula in Section F3.2.1 is chosen to predict the load-carrying capacity of ARHFB without considering its local inelastic reserve capacity. The nominal flexural strength Mnl, considering the interaction of local buckling and global buckling, is determined by Equations (7) and (8). According to the size of the dimensionless slenderness ratio of the member, different formulas are selected for calculation, and the formula for dimensionless slenderness ratio is shown in Equation (9). Where M_{ne} is the lateral torsional buckling into bending strength, M_{ol} is the

critical elastic local buckling moment, and λ_l is the dimensionless length to slenderness ratio of the member. The elastic local buckling moment M_{ol} is determined by the finite element analysis software ABAQUS.

$$\lambda_l \leq 0.776\ M_{nl} = M_{ne} \tag{7}$$

$$\lambda_l > 0.776\ M_{nl} = [1 - 0.15(\frac{M_{ol}}{M_{ne}})^{0.4}](\frac{M_{ol}}{M_{ne}})^{0.4} M_{ne} \tag{8}$$

$$\lambda_l = \sqrt{\frac{M_{ne}}{M_{ol}}} = \sqrt{\frac{M_y}{M_{ol}}} \tag{9}$$

Table 11 shows the calculation results of ARHFB using DSM. To more intuitively understand the predictive ability of DSM to ARHFB, Figures 14 and 15 are made based on the calculation results. The experimental and simulation results were compared with the DSM, respectively, and are shown in Figure 14. As seen from the figure, the data points are all located below the DSM curve. This indicates that the predictions of DSM regarding ARHFB carrying capacity are unsafe.

Table 11. Test results and comparison with the predicted results of AISI S100-2016.

Test No.	Rivet Spacing (mm)	ARHFB Sections $d_w \times b_f \times d_{f0} - d_{f1} \times t_f \times t_w$ (mm)	M_y (kN·m)	M_{ol} (kN·m)	λ_l	M_u (kN·m)		M_u/M_y	
						Test	FEM	Test	FEM
1	100	140 × 150 × 30 × 1.5 × 1.5	26.28	27.41	0.98	17.35	17.52	0.66	0.67
2		140 × 170 × 30 × 1.5 × 1.5	28.78	30.07	0.98	17.86	18.20	0.64	0.61
3		140 × 170 × 30 × 2 × 2	48.35	46.89	1.02	34.89	35.12	0.72	0.73
4		140 × 170 × 40 × 1.5 × 1.5	30.63	31.37	0.99	19.29	18.67	0.58	0.59
5		170 × 170 × 30 × 1.5 × 1.5	35.47	36.29	0.99	18.45	17.57	0.54	0.53
6		170 × 170 × 30 × 1.5 × 2	51.26	49.97	1.01	22.32	23.70	0.44	0.46
7	150	140 × 150 × 30 × 1.5 × 1.5	26.28	27.03	0.99	16.79	17.36	0.64	0.66
8	200	140 × 150 × 30 × 1.5 × 1.5	26.28	26.73	0.99	16.62	16.98	0.63	0.65

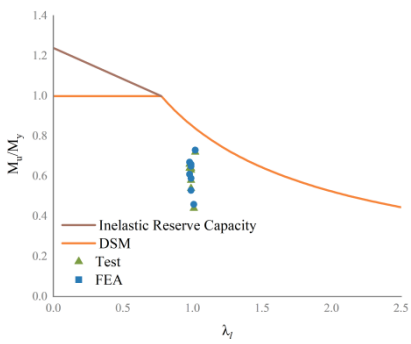

Figure 14. Comparison of test moment load capacity with AISI S100-16 predictions for the tested assembled rectangular hollow flange beams (ARHFBs).

To further discuss whether the prediction of the bearing capacity of ARHFBs by DSM is accurate, the results of the parameter study are calculated. The calculation results are recorded in Tables 8 and 9 and Figure 15. Figure 15a compares the finite element simulation results and DSM calculation results of ARHFB under different rivet spacing. From Figure 15a, it can be seen that all data points are located below the DSM curve. This is the same conclusion as the above research. Further observation of the distribution of data shows that DSM has a good predictive ability for ARHFBs with rivet spacing of 0 mm (i.e., welded connection). With the increase in rivet spacing, the prediction reliability of DSM for ARHFBs gradually decreases. This may be due to the fact that the influence of rivet spacing on the bearing capacity of ARHFBs is not considered in DSM.

According to Figure 15b, it can be seen that DSM has better prediction ability for ARHFBs with the same thickness of flange and web, namely '140 × 150 × 30 × 1.5 × 1.5' and '140 × 150 × 30 × 2 × 2'. The data points are close to the top and bottom of the curve.

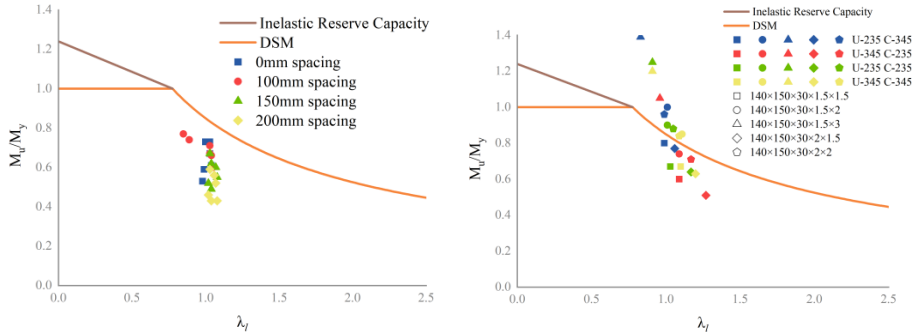

(**a**) Q235steel grade ARHFBs (**b**) 100 mm Rivet spacing ARHFBs

Figure 15. Comparison of test moment load capacity with AISC360-10 predictions for assembled rectangular hollow flange beam (ARHFB) of parameter study.

For the mixed sections with different thicknesses of web and flange, '140 × 150 × 30 × 1.5 × 2' and '140 × 150 × 30 × 1.5 × 3', the data points of '140 × 150 × 30 × 1.5 × 3' are all above the DSM curve, which means that its carrying capacity is conservatively predicted by DSM. The difference in the prediction of this bearing capacity becomes more obvious as the thickness difference between the flange and the web becomes larger. Figure 15b also shows the prediction of ARHFBs of different steel grades with the same thickness of web and flange by DSM. According to the distribution of data points in the figure, it can be seen that the green and yellow data points are closer to the DSM prediction curve. This shows that the bearing capacity of ARHFBs with the same thickness and steel grade of web and flange can be predicted by DSM more accurately. For ARHFBs with different grades of web and steel, namely 'U-235 C-345' and 'U-345 C-235', DSM is more accurate in predicting 'U-235 C-345'. In general, DSM is often unable to safely predict the carrying capacity of ARHFB. Moreover, ARHFBs with different thicknesses and different strengths of web and flange cannot be accurately predicted.

6. Conclusions

In this paper, a new type of assembling rivet-fastened hollow flange beams (ARHFBs) was proposed. The process of the four-point bending test of the ARHFBs was introduced in detail. The experimental phenomena, failure modes, and data results were analyzed. Parameter analysis was carried out by finite element software ABAQUS to determine the influence of rivet spacing, section depth, and beam span on the loading capacity of ARHFBs. The loading capacity of ARHFBs was predicted by GB50018 and AISI S100. Based on the above research, the conclusions were drawn as follows.

(1) Q235 steel with a thickness of 2 mm has a higher yield strength than steel with a thickness of 1.5 mm, but Q235 steel with a thickness of 2 mm has a shorter yield platform and lower plasticity. Q235 steel with the same thickness can also have different yield strengths due to having different plate batches.
(2) The web depth is from 140 mm to 170 mm, and the bearing capacity increased by 6%. The depth of the flange is from 30 mm to 40 mm; the bearing capacity is increased by 8%. The flange depth is only increased by 10 mm, but the bearing capacity of the ARHFB is significantly improved. Increasing the depth of the flange can effectively improve the overall loading capacity of the ARHFB.
(3) Increasing the thickness of the flange and web will improve the bearing capacity of the ARHFB. When the thickness of the web and the flange is the same, and increases from 1.5 mm to 2 mm, the bearing capacity is increased by 59%. When the flange thickness is 2 mm, the web increases from 1.5 mm to 2 mm, and the bearing capacity

is increased by 39%. While the 2 mm web thickness remains unchanged, the flange thickness increases from 1.5 mm to 2 mm, and the bearing capacity is only increased by 10%. This makes it a more economical choice to increase the thickness of the web.

(4) Increasing the strength of the flange and web can improve the bearing capacity of ARHFBs. The specimens with the strength of 'U-shape235 MPa C-shape345 MPa' are higher than those with the strength of 'U-shape345 MPa C-shape235 MPa'. The difference between the specimen with the strength of 'U-shape345 MPa C-shape345 MPa' and the specimen with the strength of 'U-shape345 MPa C-shape235 MPa' is small; the maximum is only 9%. The web strength has a greater impact on the bearing capacity of the ARHFB than the flange strength.

(5) The developed finite element model is highly consistent with the experimental results, including failure mode and ultimate load. This means that the finite element model can accurately simulate the experimental process and results, and it can be used in parameter research.

(6) According to a large number of parameter analyses, the loading capacity of 100 mm rivet spacing intermittent connection ARHFBs is only 3% lower than that of welded ARHFBs. The rivet spacing of 100 mm can be used as a more economical connection scheme in ARHFBs, which has comparable mechanical properties to ARHFBs connected by welding. The loading capacity of ARHFBs does not decrease significantly with the increased span to use ARHFBs in long-span buildings.

(7) The effective width method (EWM) and direct strength method (DSM) in AISI were used to predict the ARHFB. Among them, the EWM can predict the ARHFB more accurately with a rivet spacing of 100 mm and uniform overall strength, while the DSM is often unsafe for the prediction of ARHFB. It is recommended that GB50018 be used to predict the load-carrying capacity of ARHFBs.

Author Contributions: Conceptualization, X.C. and Q.W.; methodology, X.C. and Y.W. (Yunqing Wang); software, J.X.; validation, J.X. and Y.W. (Yifan Wang); formal analysis, J.X.; investigation, J.X.; resources, S.M., Q.W., M.A. and N.Y.; data curation, J.X. and X.C.; writing—original draft preparation, J.X.; writing—review and editing, X.C. and Q.W.; visualization, S.M., M.A. and N.Y.; supervision, S.M., M.A. and N.Y.; project administration, S.M., M.A. and N.Y.; funding acquisition, S.M. and Q.W. All authors have read and agreed to the published version of the manuscript.

Funding: This research was funded by the Postgraduate Research & Practice Innovation Program of Jiangsu Province grant number (SJCX23_2224) and the APC was funded by the Postgraduate Research & Practice Innovation Program of Jiangsu Province grant number (KYCX22_3833).

Data Availability Statement: The raw data supporting the conclusions of this article will be made available by the authors on request.

Conflicts of Interest: Author Yunqing Wang was employed by the company Plais Precision Technology (Shenzhen) Co., Ltd. The remaining authors declare that the research was conducted in the absence of any commercial or financial relationships that could be construed as a potential conflict of interest.

References

1. Chen, G.; Yang, J.; Wang, R.; Li, K.; Liu, Y.; Beer, M. Seismic damage analysis due to near-fault multipulse ground motion. *Earthq. Eng. Struct. Dyn.* **2023**, *52*, 5099–5116. [CrossRef]
2. Chen, G.; Yang, J.; Liu, Y.; Kitahara, T.; Beer, M. An energy-frequency parameter for earthquake ground motion intensity measure. *Earthq. Eng. Struct. Dyn.* **2023**, *52*, 271–284. [CrossRef]
3. Avery, P.; Mahendran, M. Finite-element analysis of hollow flange beams with web stiffeners. *J. Struct. Eng.* **1997**, *123*, 1123–1129. [CrossRef]
4. Hou, J.; Ye, Z.; Zhang, J. Research and development on the stability of beams and purlins in lightweight steel structures. *Prog. Archit. Steel Struct.* **2004**, *4*, 15–21.
5. He, B.; Zhou, T. Application of cold-formed steel structures to research in the United States. *Build. Struct.* **2001**, *31*, 58–61.
6. Dempsey, R.I. Structural behavior and design of hollow flange beams. In *Second National Structural Engineering Conference 1990: Preprints of Papers*; National Conference Publication; Institution of Engineers, Australia: Barton, ACT, Australia, 1990; pp. 327–335.

7. Hassanein, M.F.; Kharoob, O.F. Shear strength and behavior of transversely stiffened tubular flange plate girders. *Eng. Struct.* **2010**, *32*, 2617–2630. [CrossRef]
8. Anapayan, T.; Mahendran, M.; Mahaarachchi, D. Lateral distortional buckling tests of a new hollow flange channel beam. *Thin-Walled Struct.* **2011**, *49*, 13–25. [CrossRef]
9. Hasanein, M.F.; Kharoob, O.F. An extended evaluation for the shear behavior of hollow tubular flange plate girders. *Thin-Walled Struct.* **2012**, *56*, 88–102. [CrossRef]
10. Beg, D.; Kuhlmann, U.; Davaine, L.; Braun, B. *Design of Plated Structures: Eurocode 3: Design of Steel Structures, Part 1–5: Design of Plated Structures*; John Wiley & Sons: Hoboken, NJ, USA, 2012.
11. Hassanein, M.F.; Silvestre, N. Lateral–distortional buckling of hollow tubular flange plate girders with slender unstiffened webs. *Eng. Struct.* **2013**, *56*, 572–584. [CrossRef]
12. Hasanein, M.F.; Kharoob, O.F. Flexural strength of hollow tubular flange plate girders with slender stiffened webs under mid-span concentrated loads. *Thin-Walled Struct.* **2013**, *69*, 18–28. [CrossRef]
13. Mohebkhah, A.; Azandariani, M.G. Lateral–torsional buckling of delta hollow flange beams under moment gradient. *Thin-Walled Struct.* **2015**, *86*, 167–173. [CrossRef]
14. Peters, G.K. An Investigation of the Effects of Fastened Spacing in Build-Up Cold-Formed Steel Compression Members. Master's Thesis, Dalhousie University, Halifax, NS, Canada, 2003.
15. Abbasi, M.; Khezri, M.; Rasmussen, K.J.R. Elastic buckling analysis of cold-formed steel built-up sections with discrete fasteners using the compound strip method. *Thin-Walled Struct.* **2018**, *124*, 58–71. [CrossRef]
16. *GB 50018-2002*; Technical Code of Cold-Formed Thin-Wall Steel Structure. China Architecture and Building Press: Beijing, China, 2002. (In Chinese)
17. American Iron and Steel Institute; Committee on Specifications, Canadian Standards Association; Technical Committee on Cold Formed Steel Structural Members, Messico; Camara Nacional de la Industria del Hierro y del Acero. *North American Specification for the Design of Cold-Formed Steel Structural Members*; American Iron and Steel Institute: Washington, DC, USA, 2016.
18. *GB/T 228.1-2010*; Metallic Materials-Tensile Testing-Part 1: Method of Test at Room Temperature. China Standards Press: Beijing, China, 2010. (In Chinese)
19. *Abaqus 2020*; SIMULIA; Dassault Systèmes: Vélizy-Villacoublay, France, 2020.
20. Paczos, P. Experimental and numerical (FSM) investigations of thin-walled beams with double-fox flanges. *J. Theor. Appl. Mech.* **2013**, *51*, 497–504.
21. Sudhir Sastry, Y.B.; Krishna, Y.; Budarapu, P.R. Parametric studies on buckling of thin walled channel beams. *Comput. Mater. Sci.* **2015**, *96 Pt B*, 416–424. [CrossRef]
22. Dong, J.; Sause, R. Behavior of hollow tubular-flange girder systems for curved bridges. *J. Struct. Eng.* **2010**, *136*, 174–182. [CrossRef]
23. Siahaan, R.; Keerthan, P.; Mahendran, M. Finite element modeling of rivet fastened rectangular hollow flange channel beams subject to local buckling. *Eng. Struct.* **2016**, *126*, 311–327. [CrossRef]
24. Xue, J.; Ma, S.; Chen, X.; Wu, Q.; Akbar, M. Finite element modeling of assembling rivet-fastened rectangular hollow flange beams in bending. *J. Constr. Steel Res.* **2023**, *211*, 108177. [CrossRef]
25. *GB 50017-2017*; Code for Design of Steel Structures. China Architecture and Building Press: Beijing, China, 2018. (In Chinese)